The Pennsylvania State University
The Graduate School
Department of Chemistry

CALCULATION OF ABSOLUTE RESONANCE RAMAN INTENSITIES

A Thesis in
Chemistry
by
Krista A. Kane

Submitted in Partial Fulfillment
of the Requirements
for the Degree of

Master of Science

December 2009

The thesis of Krista A. Kane was reviewed and approved* by the following:

Lasse Jensen
Assistant Professor of Chemistry
Thesis Advisor

John V. Badding
Professor of Chemistry

Mark Maroncelli
Professor of Chemistry

Barbara Garrison
Shapiro Professor of Chemistry
Head, Department of Chemistry

*Signatures are on file in the Graduate School.

Abstract

We present the resonance Raman (RR) spectra of uracil, rhodamine 6G (R6G) and iron(II) porphyrin with imidazole and CO ligands (FePImCO) calculated using density functional theory (DFT). The absolute RR intensities were determined using both the vibronic theory and the short-time approximation. We found that the absolute RR intensities calculated using the short-time approximation are overestimated compared to those calculated using the vibronic theory. This is attributed to the sensitivity of the short-time approximation to the damping parameter. Uracil is not affected by vibronic coupling and so the absolute RR intensities calculated using both methods should be comparable. Despite the agreement obtained in the relative RR intensities, the absolute RR intensities calculated using the short-time approximation are severely overestimated compared to those calculated using the vibronic theory. In addition, the absolute RR intensities of R6G, computed using the vibronic theory, are only slightly underestimated compared to experiment, which is attributed to the neglect of solvent effects in the calculations. The absolute RR intensities calculated using vibronic theory correctly resulted in an increase in the relative RR intensity of the low-frequency Raman bands for molecules that experience vibronic coupling (i.e. R6G and FePImCO), but was not observed in the RR spectra calculated using the short-time approximation.

Table of Contents

List of Figures

List of Tables

Acknowledgments

I would like to thank Lasse Jensen for his guidance and support on my research at Penn State. I would also like to thank the entire Jensen group, especially Seth Morton for all of his help. I would like to thank my committee members: Dr. John Badding, Dr. Mark Maroncelli, and Dr. Coray Colina for taking the time to be on my committee. Last, but not least, I would also like to thank my family and friends for their continued love and support.

Chapter 1

Introduction

1.1 Background

Biological macromolecules participate in processes that are the foundation of survival for living organisms.[1,2] One particular class of biological macromolecules that we are interested in is metalloproteins. Metalloproteins function as enzymes, transport and storage proteins, and signal transduction proteins.[1–4] An example of a metalloprotein is chlorophyll, which plays a role in energy conversion in plants.[3,5] One specific group of metalloproteins is the heme protein, whose active site consists of a porphyrin ring bound to a central iron atom. Heme proteins perform many functions that are vital for living organisms. For example, myoglobin and hemoglobin are heme proteins that are responsible for oxygen storage and transport,[3,6–9] cytochromes b and c are heme proteins that participate in electron transport,[3,10] and cytochrome P450 and cytochrome oxidase function in oxygen activation and utilization.[3,11] In order to gain new insights into the structure and function of heme proteins, theorists calculate and analyze the vibrational spectra of metalloporphyrins that model heme protein active sites.[1–3,8,9]

Porphyrins have applications other than biological functions. For example, porphyrins are being considered as catalysts for chemical and photochemical reactions.[3] Additionally, porphyrins have potential technological applications in electronics, optoelectronics, and photonics.[12,13] For example, metalloporphyrins have recently been used in the design of a molecular photonic wire that absorbs a photon of visible light and subsequently outputs the photon at the other end of the wire.[13]

The ability of metalloporphyrins to undergo oxidation/reduction allows them to act as the off/on "switching element" in the molecular photonic wire. Zinc porphyrins are being investigated for their applications in dye-sensitized solar cells (DSSCs).[14,15]

The function of biological macromolecules is dictated by their specific three-dimensional structure.[4] One tool we use to investigate biologically relevant molecules is vibrational spectroscopy. One advantage of vibrational spectroscopy over other spectroscopic techniques is that it can provide detailed structural information that can be used to identify compounds, unlike UV-vis absorption and fluorescence.[2] Although X-ray crystallography and nuclear magnetic resonance (NMR) spectroscopy can be used to obtain structural information, vibrational spectroscopy can also provide information about dynamics.[2] A second advantage is that vibrational spectroscopy can be used to analyze samples that are in solid, liquid, or gas states or even in monolayers.[2] This is beneficial because it allows us to obtain information about molecules in their native states. In particular, many biological macromolecules exist in an aqueous environment and so vibrational spectroscopy allows us to analyze them in their natural surroundings.

The two main vibrational spectroscopy techniques are infrared (IR) and Raman spectroscopy.[2] As the size of the molecule of interest increases, the number of vibrational modes also increases, which complicates the vibrational spectra. There are 3N-5 vibrational modes for linear molecules (3 translational and 2 rotational) and 3N-6 vibrational modes for non-linear molecules (3 translational and 3 rotational), where N is the number of atoms.[2,16,17] As a result of the increasing number of vibrational bands with larger molecules, the IR and Raman spectra become more complex and the individual bands become difficult to identify. In this case, resonance Raman spectroscopy (RRS) can be used to selectively enhance vibrational bands related to a specific chromophore within the much larger biological macromolecule of interest.[2,16–24] As a result, an understanding of how the properties of the chromophore contribute to the overall function of the protein can be obtained.

The sensitivity and selectivity of RRS makes it a powerful tool with a variety of applications. RRS is particularly useful for studying biological systems because it can be used as a tool to probe the structure and dynamics of a particular excited state associated with a specific chromophore in a much larger protein.[25] RRS is

useful in the characterization of peptide and protein secondary structure because excitation of the $\pi \rightarrow \pi^*$ transition of the peptide backbone leads to an enhancement of the amide vibrations.[26,27] A recent article in Chemical & Engineering News (C&EN) reviewed the application of IR and RRS to investigate amyloids, which are protein clumps that are related to neurological diseases, such as Alzheimer's and Parkinson's.[28] Structural information about amyloids can be obtained from X-ray crystallography and solid-state NMR, however these techniques cannot be used to study intermediate states of species, which are suspected to be responsible for these diseases. In contrast, deep-ultraviolet RRS can be used to analyze the structure and fibrilization mechanism of amyloids. In addition, RRS can be used to structurally characterize carbon nanotubes.[29–31]

1.2 Raman Spectroscopy

Raman spectroscopy is a powerful tool for analyzing molecular vibrational frequencies.[16,17] In Raman spectroscopy, a photon interacts with a molecule which results in the photon being remitted with either the same energy or a different energy as the original photon. Most of the photons given off by the molecule have the same energy as the incident photon. This process is known as elastic or Rayleigh scattering. However, a small fraction of the photons (one in one million) will be remitted with an energy different from the incident photon. This process is known as inelastic or Raman scattering. The difference in energy between the emitted and incident photon corresponds to a vibrational normal mode frequency. The vibrations can provide detailed information about chemical bonds leading to an understanding of the ground state structure and dynamics of a molecular system.

The peaks in a Raman spectrum are known as either Stokes or anti-Stokes lines depending on if the energy difference between the original and remitted photon is positive or negative, respectively.[16,17] Stokes lines represent a transition from a lower vibrational level in the ground electronic state to a higher vibrational level of the ground electronic state. This process requires the molecule to absorb some energy from the incident photon and the emitted photon therefore has less energy than the original photon. In contrast, anti-Stokes lines represent a transition from a higher vibrational level of the ground electronic state to a lower vibrational level

of the ground electronic state. Thus, energy is given off in this type of transition and the emitted photon therefore has more energy than the original photon. Stokes lines are more intense than anti-Stokes lines because they represent a transition beginning from a more populated state. It is therefore common to only present the Stokes lines in a Raman spectrum.

Sir Chandrasekhara Venakta Raman discovered the Raman effect in 1928.[16,17] Raman's interest in light scattering began with his curiosity about the blue color of the Mediterranean sea. Raman showed that the sea's color is a result of the light scattering by water molecules. Subsequently, Raman investigated the scattering of light by water and other liquids and for all of the molecules studied, described his observations as a "feeble fluorescence" because they produced such a weak signal. Raman scattering was an immediate sensation; as around 70 papers concerning the Raman effect had been published by the end of 1928.[17] Raman was awarded the Nobel Prize in physics in 1930.[17] Raman spectroscopy became a more active field of study with the advent of the laser in the early to mid-1960's because lasers emit light of a single wavelength, producing more concentrated photons, and as a result a stronger signal.[16,17]

Both Raman and infrared (IR) spectroscopy can be used to investigate vibrational transitions in molecules.[16,17,32] The vibrational frequencies that appear in the Raman and IR spectrum may differ from one another as a result of the symmetry of the molecule. The Raman and IR spectra are specific for the molecule of interest. For this reason, the application of both Raman and IR spectroscopy is a useful tool for the identification of unknown compounds. While Raman spectroscopy is a two-photon process, IR spectroscopy is a one photon event. IR absorption is due to a resonance between the frequency of the incident IR radiation and the vibrational frequency of a certain normal mode of vibration. Molecules that are IR active experience a change in dipole moment with respect to its vibrational motion. In contrast, molecules that are Raman active undergo a change in polarizability with respect to its vibrational motion.

Although similar information is obtained from both Raman and IR spectroscopy, differences among these two techniques can be identified in the energy-level diagram, shown in Figure 1.1. For both Stokes Raman scattering and IR absorption, the initial state is the zeroth vibrational level of the ground electronic

state and the final state is the first vibrational level of the ground electronic state. However, as depicted in the energy-level diagram, IR spectroscopy is a result of a direct excitation from the zeroth vibrational level of the ground electronic state to the first vibrational level of the ground electronic state, whereas Raman scattering is not a result of a direct excitation, but rather involves an excitation to an intermediate virtual energy state. In other words, IR absorption is a one-photon event, whereas Raman scattering is a two-photon process. The figure also illustrates Rayleigh scattering, where the initial and final states are both the zeroth vibrational level of the ground electronic state, and Anti-Stokes Raman scattering, where the initial state is the first vibrational level of the ground electronic state and the final state is the zeroth vibrational level of the ground electronic state.

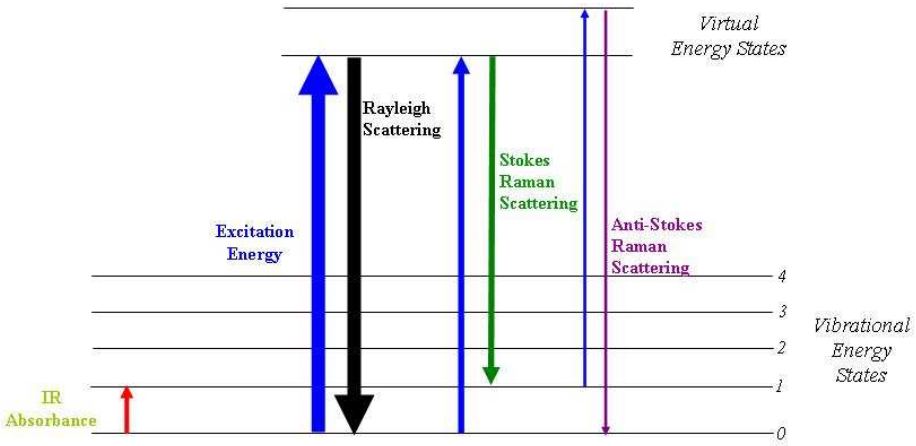

Figure 1.1. Energy-level diagram for IR absorption, Rayleigh Scattering, Stokes Raman Scattering, and Anti-Stokes Raman Scattering. Image taken from *http* : *//en.wikipedia.org/wiki/File* : *Raman_energy_levels.jpg*.

Raman spectroscopy has several advantages over IR spectroscopy.[32] First, the small diameter of the laser beam decreases the amount of sample area needed. Also, Raman spectra can be obtained from aqueous solutions easily because water does not result in interference. In contrast, water shows a strong absorption band in the IR spectrum. Since many biological systems exist in aqueous environments, this feature allows Raman spectroscopy to have many biological applications. Lastly,

Raman spectra can be obtained from air-sensitive compounds by utilizing a sealed glass tube. In IR spectroscopy, the glass tube would interfere with the signal because it absorbs IR radiation. The main disadvantages of Raman spectroscopy are that the signal is weak and also the use of a laser can lead to fluorescence in the spectrum, which can conceal the Raman bands.[32]

1.3 Resonance Raman Spectroscopy

Resonance Raman spectroscopy (RRS) can be used to enhance molecular vibrational frequencies due to a particular electronic transition by a factor of as much as 10^6.[16–24] In RRS the incident light is adjusted to a specific energy that corresponds with the energy of the electronic transition of interest for a particular molecule. As a result, only the vibrational frequencies associated with that specific electronic transition are evident in the RR spectrum. Thus, RRS can provide information about the excited state structure and dynamics. Theoretical calculations of the RR spectrum are useful in the determination of these properties, whereas it may be difficult to ascertain this information from experimental data.[33,34] Furthermore, comparison of the theoretical RR spectrum with the experimental RR spectrum can lead to the improvement of the theoretical methods utilized to calculate RR spectra.[33] Figure 1.2 gives a general energy-level diagram for pre-resonance and resonance Raman spectroscopy.

1.4 Objective

A frequent trend is to simply determine the relative RR intensities, which is acceptable in order to analyze and assign the RR spectra. However, we are interested in determining the absolute RR intensities presented as differential cross-sections. Determination of the absolute RR intensities is necessary in order to assess the enhancement factors in surface enhanced resonance Raman spectroscopy (SERRS).[35,36] We have used density functional theory (DFT) to calculate the RR spectra using two different theoretical methods: vibronic theory[18–20,37–39] and short-time approximation.[21,22,40] While implementation of the short-time approximation is much simpler than the vibronic theory, it's validity in the determination of the ab-

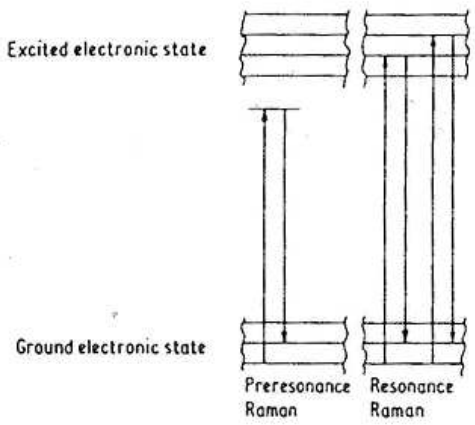

Figure 1.2. Energy-level diagram for pre-resonance and resonance Raman spectroscopy. Image taken from $http://www.sicklecellinfo.net/images/research/raman.3.gif$.

solute RR intensities has yet to be determined. The main difference between the two methods is that the vibronic theory takes into account vibronic coupling terms, which are due to the interaction between vibrational and electronic modes. Comparison of the RR differential cross-sections obtained using each of these methods can provide insight into the accuracy of the short-time approximation.

Several test systems are used to determine the accuracy and consistency of the vibronic model that we implemented. Initially, the Raman differential cross-sections of 2-bromo-2-methylpropane (2B2MP) are determined and compared to both experimental[41] and theoretical[36] results available in the literature. Subsequently, the RR differential and total cross-sections of carbon disulfide (CS_2) are calculated and compared to experimental results.[42] The RR differential cross-sections for the S_2 state of uracil are determined using the short-time approximation and are compared to the differential cross-sections obtained using the polarizability gradient model derived by Jensen et al.[43] In principle, the differential cross-sections calculated using the short-time approximation and the polarizability gradient model should be comparable, since they are both computed using a single excited state. In addition, we will compare the absolute intensities obtained using the short-time approximation and the polarizability gradient model with those obtained using the vibronic model. Rhodamine 6G (R6G) is affected by vibronic

coupling and so this is an ideal system to observe the vibronic coupling effects in the RR spectrum.[33] As a result, we would expect to observe differences in the RR differential cross-sections calculated using the two different methods under investigation. Furthermore, experimental absolute intensities have recently been reported.[35] Iron(II) porphyrin with imidazole and CO ligands (FePImCO) is used as a model system for understanding larger biologically relevant molecules containing a heme group, such as myoglobin, hemoglobin, or cytochrome c.[8] FePImCO experiences vibronic coupling and will be an interesting case used to investigate the accuracy of the intensities derived from the vibronic versus the short-time approximation.

Chapter 2

Theoretical Methods

2.1 Background

In this chapter, we review the basic aspects of RR scattering theory. In 1925, Hendrik Kramers and Werner Heisenberg developed the Kramers-Heisenberg dispersion formula, which describes the scattering cross-section of a photon by an atomic electron.[44] In 1927, Paul Dirac developed the quantum mechanical derivation for this equation using perturbation theory.[45] Due to the complexity of the Kramers-Heisenberg-Dirac (KHD) formalism, several different approximations to the KHD formalism have been proposed. The two main simplifications to the KHD formalism are the vibronic theory and the time-dependent approach. We will discuss both of these methods in this chapter.

2.2 Vibronic Theory

The vibronic theory[18–20,37–39] was introduced by Albrecht and co-workers.[18–20] The vibronic theory uses the Born-Oppenheimer approximation, which separates the vibronic states into products of electronic and vibrational states. Subsequently, the transition dipole moment is expanded in a Taylor series in the nuclear coordinates. The result of the expansion is a sum of different terms, known as the Albrecht A,B,C, and D terms, that contribute to the RR intensities. The A term corresponds to the Franck-Condon type scattering, which describes the RR intensity based on the electronic transition dipole moment and also the vibrational overlap integrals.

Therefore, the Franck-Condon mechanism is most important for strong transitions that have large dipole moments and large vibrational overlap integrals. The B term describes the Herzberg-Teller type scattering, which involves the vibronic coupling between two excited electronic states. This term is neglected because taking into consideration coupling to more than one excited electronic state is rarely necessary. The C term takes into account the vibronic coupling between the ground electronic state and an excited electronic state. The C term is considered to be negligible because of the large energy separation between the ground and excited electronic states. Finally, the D term considers the vibronic coupling between an excited electronic state to two other excited states. This term is likely to be small and is therefore not considered. Each of these terms is expressed as a sum over intermediate vibrational states in the resonant excited electronic state. As a result, the calculation becomes computationally challenging for larger molecules with many vibrational modes.[17]

In order to further simplify the vibronic theory, five assumptions are introduced. First, the Born-Oppenheimer approximation is utilized. The Born-Oppenheimer approximation states that since the the electrons are so much less massive than the nuclei, the electrons move much faster than the nuclei and the electronic and nuclear motion can therefore be separated. Second, only Franck-Condon-type scattering is considered. Since the nuclei move much more slowly than the electrons, the electronic transitions are considered to be vertical transitions. Third, the excitation frequency is in resonance with only one excited state. Fourth, the ground and excited electronic state potential energy surfaces are considered to be harmonic. Last, the excited and ground electronic state normal coordinates vary from one another only by their equilibrium positions so that the frequencies for the ground and excited state vibrations are the same. These assumptions lead to the consideration of only the Albrecht A term, which for vibrational RR scattering is of the form:

$$[\alpha(\omega_L)]_{f,i} = \mu^2 \sum_{\nu} \frac{\langle f|\nu\rangle \langle \nu|i\rangle}{\omega_{\nu i} - \omega_L - i\Gamma} \tag{2.1}$$

where $\alpha(\omega_L)$ is the polarizability tensor, μ is the electronic transition dipole moment, $|f\rangle$ is the final vibrational level of the ground electronic state, $|i\rangle$ is the initial vibrational level of the ground electronic state, $|\nu\rangle$ is the intermediate vibrational

level of the excited electronic state, ω_L is the frequency of the incident radiation, Γ is the line width (half width at half maximum of the absorption band), and $\omega_{\nu i}$ is the frequency associated with the normal mode of interest. The polarizability tensor can be expanded in terms of the normal modes to give:

$$[\alpha(\omega_L)]_{f,i} = \mu^2 \sum_{\nu_1} ... \sum_{\nu_{3N-6}} \frac{\langle f_1|\nu_1\rangle \langle \nu_1|i_1\rangle \prod_{j=2}^{3N-6} |\langle \nu_j|0_j\rangle|^2}{\omega_0 + \sum_j^{3N-6} \nu_j\omega_j - \omega_L - i\Gamma} \tag{2.2}$$

where $\omega_{\nu i}$ is given by:

$$\omega_{\nu i} = \omega_0 + \sum_{j=1}^{3N-6} \nu_j\omega_j \tag{2.3}$$

where ω_0 is the frequency corresponding to the transition from the ground electronic state to the resonant electronic state for the zeroth vibrational level, ω_j is the frequency of the j^{th} normal mode, and ν_j is the vibrational quantum number of the j^{th} normal mode. The term $|\langle \nu_j|0_j\rangle|^2$ is also known as the Franck-Condon term, which will be discussed in more depth later in this chapter. In equation 2.2, the subscript 1 denotes the normal mode of interest. The RR intensity is proportional to the square of the polarizability tensor.

2.2.1 Transform Theory

The original transform theory was derived by Hizhnyakov and Tehver[46] and involves utilizing the experimental absorption spectrum and the Kramers-Kronig transform of the experimental absorption spectrum in order to determine the RR intensities. The absorption cross-section is given by:

$$\sigma_A(\omega_L) \propto \omega_L \mathrm{Im}([\alpha_{xx}(\omega_L)]_{0,0} + [\alpha_{yy}(\omega_L)]_{0,0} + [\alpha_{zz}(\omega_L)]_{0,0}) \tag{2.4}$$

After substituting equation 2.2 into equation 2.4 and averaging over the various molecular orientations, the absorption cross-section can be rewritten as:

$$\sigma_A(\omega_L) = \omega_L\mu^2 \sum_{\nu_1} |\langle \nu_1|0_1\rangle|^2 \sum_{\nu_2} ... \sum_{\nu_{3N-6}} \frac{\prod_{j=2}^{3N-6} |\langle \nu_j|0_j\rangle|^2 \Gamma}{\left(\omega_0 + \sum_{j=1}^{3N-6} \nu_j\omega_j - \omega_L\right)^2 + \Gamma^2} \tag{2.5}$$

Applying the intensity shift function to equation 2.5, which simply results in a slightly shifted absorption spectrum, gives:

$$S(\omega_L - \nu_1\omega_1) = \sum_{\nu_2} ... \sum_{\nu_{3N-6}} \frac{\prod_{j=2}^{3N-6} |\langle \nu_j|0_j\rangle|^2 \Gamma}{\left(\omega_0 - (\omega_L - \nu_1\omega_1) + \sum_{j=2}^{3N-6} \nu_j\omega_j\right)^2 + \Gamma^2} \tag{2.6}$$

The Kramers-Kronig transform of the intensity shift function is given by:

$$T(\omega_L - \nu_1\Omega_1) = \sum_{\nu_1} ... \sum_{\nu_{3N-6}} \frac{\prod_{j=2}^{3N-6} |\langle \nu_j|0_j\rangle|^2 (\omega_0 - (\omega_L - \nu_1\omega_1) + \sum_{j=2}^{3N-6} \nu_j\omega_j)}{(\omega_0 - (\omega_L - \nu_1\omega_1) + \sum_{j=2}^{3N-6} \nu_j\omega_j)^2 + \Gamma^2} \tag{2.7}$$

Using the definition of the intensity shift function, the absorption cross-section can be rewritten as:

$$\sigma_A(\omega_L) \propto \omega_L \mu^2 \sum_{\nu_1} |\langle \nu_1|0_1\rangle|^2 S(\omega_L - \nu_1\omega_1) \tag{2.8}$$

Substituting the intensity shift function and the Kramers-Kronig transform into equation 2.2 gives the polarizability tensor for the $i_1 \rightarrow f_1$ transition:

$$[\alpha(\omega_L)]_{f,i} = \mu^2 \left[\sum_{\nu_1} \langle 1_1|\nu_1\rangle \langle \nu_1|0_1\rangle T(\omega_L - \nu_1\omega_1) + i \sum_{\nu_1} \langle 1_1|\nu_1\rangle \langle \nu_1|0_1\rangle S(\omega_L - \nu_1\omega_1) \right] \tag{2.9}$$

where the polarizability tensor has been separated into real and imaginary parts.

The Franck-Condon factors can be expressed in terms of the dimensionless displacements, represented by Δ, of the excited state equilibrium structure. The dimensionless displacement is the change in the excited state equilibrium position relative to the ground state equilibrium position along the normal coordinate of vibration j. Figure 2.1 pictorially defines the dimensionless displacement. Several

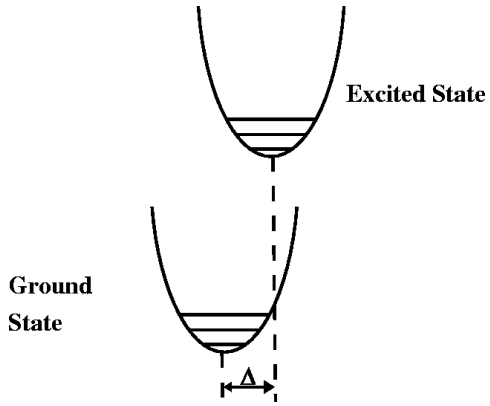

Figure 2.1. Pictorial definition of the dimensionless displacement, Δ.

general expressions for various Franck-Condon factors are given by[47]:

$$|\langle \nu_j|0_j\rangle|^2 = \frac{\Delta_j^{2\nu_j}}{2^{\nu_j}\nu_j!}e^{-\Delta_j^2/2} \tag{2.10}$$

$$|\langle 0_j|\nu_j-1\rangle|^2 = \frac{\Delta_j^{2(\nu_j-1)}}{2^{\nu_j-1}(\nu_j-1)!}\frac{2\nu_j}{2\nu_j}e^{-\Delta_j^2/2} = \frac{2\nu_j\Delta_j^{2\nu_j-2}}{2^{\nu_j}\nu_j!}e^{-\Delta_j^2/2} \tag{2.11}$$

$$\langle 1_j|\nu_j\rangle\langle \nu_j|0_j\rangle = \frac{\Delta_j}{\sqrt{2}}\left[\frac{\Delta_j^{2\nu_j}}{2^{\nu_j}\nu_j!} - \frac{2\nu_j\Delta_j^{2\nu_j-2}}{2^{\nu_j}\nu_j!}\right]e^{-\Delta_j^2/2} \tag{2.12}$$

Thus, the Franck-Condon factors can be solved for analytically using the dimensionless displacements. The following relationship can be obtained from equation 2.10 through equation 2.12:

$$\langle 1_j|\nu_j\rangle\langle \nu_j|0_j\rangle = \frac{\Delta_j}{\sqrt{2}}\left[|\langle 0|\nu_j\rangle|^2 - |\langle 0|\nu_j-1\rangle|^2\right] \tag{2.13}$$

Expressing the Franck-Condon factors in terms of the dimensionless displacements allows us to rewrite the polarizability tensor for the $i_1 \rightarrow f_1$ transition according to:

$$[\alpha(\omega_L)]_{f,i} = \mu^2\frac{\Delta_1}{\sqrt{2}}\left[\sum_{\nu_1\geq 0}\langle 0_1|\nu_1\rangle^2\left(T(\omega_L-\nu_1\omega_1)+iS(\omega_L-\nu_1\omega_1)\right)\right.$$

$$- \sum_{\nu_1 \geq 0} \langle 0_1 | \nu_1 \rangle^2 \left(T(\omega_L - (\nu_1 + 1)\omega_1) + iS(\omega_L - (\nu_1 + 1)\omega_1) \right) \Bigg] \quad (2.14)$$

The polarizability tensor and absorption cross-section can be given as:

$$[\alpha(\omega_L)] \propto \mu^2 \frac{\Delta_1}{\sqrt{2}} [\Phi(\omega_L) - \Phi(\omega_L - \omega_1)] \quad (2.15)$$

and

$$\sigma_A(\omega_L) \propto \omega_L \mu^2 \mathrm{Im}\Phi(\omega_L) \quad (2.16)$$

where the function $\Phi(\omega_L)$ is given by:

$$\Phi(\omega_L) = \sum_{\nu_1} | \langle 0_1 | \nu_1 \rangle |^2 (T(\omega_L - \nu_1\omega_1) + iS(\omega_L - \nu_1\omega_1)) \quad (2.17)$$

Since the square of the polarizability tensor is equivalent to the relative RR intensity, the RR intensity for the transition from the ground electronic state, $|i\rangle$, to the final vibrational level of the ground electronic state, $|f\rangle$, for normal mode j is given by:

$$I_j(\omega_L) = \mu^4 \frac{\Delta_j^2}{2} |\Phi(\omega_L) - \Phi(\omega_L - \omega_j)|^2 \quad (2.18)$$

In the original transform theory, the quantity $|\Phi(\omega_L) - \Phi(\omega_L - \omega_j)|^2$, given in equation 2.18, is determined from the experimental absorption spectrum and its Kramers-Kronig transform. Since the real and imaginary parts of $\Phi(\omega_L)$ form a Kramers-Kronig transform pair, the imaginary part of $\Phi(\omega_L)$ that is obtained from the experimental absorption spectrum can be used to solve for the imaginary part of $\Phi(\omega_L)$ using the Cauchy principle-value integral which relates the real and imaginary parts of $\Phi(\omega_L)$.

The method we used to calculate the RR intensities is based on the transform theory derived by Peticolas and Rush.[48] This method was also adopted more recently by Neugebauer and Hess[49] and also Guthmuller and Champagne.[33,34] According to this theoretical approach, the quantity $|\Phi(\omega_L) - \Phi(\omega_L - \omega_j)|^2$ was calculated from the sum-over-vibrational states where $\Phi(\omega_L)$ is given by:

$$\Phi(\omega_L) = \sum_{\nu} \frac{\prod_j^{3N-6} | \langle \nu_j | 0_j \rangle |^2}{\omega_0 + \sum_j^{3N-6} \nu_j\omega_j - \omega_L - i\Gamma} \quad (2.19)$$

The equation used to solve for $\Phi(\omega_L)$, equation 2.19, is identical to the polarizability tensor given by the vibronic theory, equation 2.1. Thus, from a theoretical perspective, the transform theory is synonymous with the vibronic theory. All of the quantities involved in equations 2.18 and 2.19 are determined from quantum chemical calculations, except for Γ. As already mentioned, Γ is the line width of the absorption band (equal to half of the full width at half maximum). Thus, Γ is inversely proportional to the lifetime. Γ is an adjustable parameter, whose value can be approximated from the experimental absorption spectrum. Finally, the absorption spectra and RR spectra were calculated using Equations 2.16 and 2.18, respectively.

2.2.2 Short-time Approximation

A simplification of the vibronic theory is the short-time approximation.[21,22,40] Within the short-time approximation, the RR intensity for normal mode j is given by:

$$I_j = \left(\frac{\mu}{\Gamma}\right)^4 \omega_j^2 \Delta_j^2 \tag{2.20}$$

where μ is the electronic transition dipole moment, Γ is the adjustable damping parameter, ω_j is the frequency of normal mode j, and Δ_j is the dimensionless displacement of normal mode j. Assuming displaced harmonic oscillators, the relative RR intensities are equal to the square of the excited state gradient, according to:

$$\left(\frac{\partial E}{\partial q_j}\right)_{q_j=0} = \omega_j(q_j - \Delta_j)|_{q_j=0} = -\omega_j \Delta_j \tag{2.21}$$

where $\left(\frac{\partial E}{\partial q_j}\right)_{q_j=0}$ is the partial derivative of the excited state electronic energy with respect to a ground state normal mode at the ground state equilibrium position. Note that the RR intensity, calculated using the short-time approximation, is independent of the frequency of the incident radiation.

2.2.3 Polarizability Gradient Model

The RR spectra calculated using the short-time approximation and the vibronic theory for uracil are compared to the RR spectra calculated using the polarizabil-

ity gradient model developed by Jensen et al.[43] Using the polarizability gradient model, we calculate the RR intensities from the derivative of the real and imaginary parts of the frequency-dependent polarizability with respect to the normal coordinates. Within the polarizability gradient model, the RR scattering factor is given by:

$$I_j = 45\alpha_j'^2 + 7\gamma_j'^2 \tag{2.22}$$

where $\alpha_p'^2$ is the derivative of the isotropic polarizability with respect to normal mode j and $\gamma_j'^2$ is the derivative of the anisotropic polarizability with respect to normal mode j.

2.2.4 RR Differential Cross-Sections

The absolute RR intensities are presented as the differential RR cross-section (units of cm^2/sr). The differential cross-section for Stokes scattering is given by:

$$\frac{d\sigma}{d\Omega} = K_j \left[\frac{12I_j}{45}\right] \tag{2.23}$$

where I_j is the RR scattering factor obtained from equation 2.18, equation 2.20, or equation 2.22 in units of Å^4/amu and K_j is given by:

$$K_j = \frac{\pi^2}{\epsilon_0^2}(\tilde{\nu_L} - \tilde{\nu_j})^4 \left(\frac{h}{8\pi^2 c\tilde{\nu_j}}\right)\left(\frac{1}{1 - e^{-\frac{hc\tilde{\nu_j}}{k_B T}}}\right) \tag{2.24}$$

where ϵ_0 is the permittivity of vacuum, c is the speed of light in units of m/s, h is the Planck constant, k_B is the Boltzmann constant, T is the temperature (taken to be 300 K), $\tilde{\nu_L}$ is the frequency of the incident radiation in units of cm^{-1}, and $\tilde{\nu_j}$ is the frequency of normal mode j in units of cm^{-1}.[43,50]

2.3 Time-Dependent Approach

Another method for the calculation of RR intensities is the time-dependent approach[21,23,24,51,52] derived by Heller and co-workers. The advantage of the time-dependent approach is that the need to perform a computationally challenging sum over the excited vibrational states is eliminated by taking into consideration

the time dependence of the RR scattering phenomenon. Starting with the polarizability tensor given by equation 2.1, where we have substituted $\hbar\omega_{\nu i} = E_\nu - E_i$ and $\hbar\omega_L = E_L$, we have:

$$[\alpha(\omega_L)]_{f,i} = \mu^2 \sum_\nu \frac{\langle f|\nu\rangle \langle \nu|i\rangle}{(E_\nu - E_i - E_L - i\Gamma)} \tag{2.25}$$

First, the sum over states polarizability tensor is converted into a fully equivalent time-dependent formulation. The denominator in Equation 2.25 is expressed as a half-Fourier transform to obtain:

$$[\alpha(\omega)]_{f,i} = \mu^2 \frac{i}{\hbar} \int_0^\infty \sum_\nu \langle f|\nu\rangle \langle \nu|i\rangle \, e^{[i(E_L+E_i-E_\nu+\Gamma)t/\hbar]} dt \tag{2.26}$$

Next since $\langle \nu|e^{-iHt/\hbar} = \langle \nu|e^{-iE\nu t/\hbar}$, where H is the excited state vibrational Hamiltonian, we have:

$$[\alpha(\omega_L)]_{f,i} = \mu^2 \frac{i}{\hbar} \int_0^\infty \sum_\nu \langle f|\nu\rangle \left\langle \nu|e^{-iHt/\hbar}|i\right\rangle e^{[i(E_L+E_i+\Gamma)t/\hbar]} dt \tag{2.27}$$

If we consider the time-propagator $e^{-iHt/\hbar}$ to operate on $|i\rangle$, then $e^{-iHt/\hbar}|i\rangle = |i(t)\rangle$. The complete expression for the polarizability tensor is then:

$$[\alpha(\omega_L)]_{f,i} = \mu^2 \frac{i}{\hbar} \int_0^\infty \langle f|i(t)\rangle \, e^{[i(E_L+E_i+\Gamma)t/\hbar]} dt \tag{2.28}$$

Since the RR intensity is proportional to the square of the polarizability tensor, we have:

$$I_{i\to f} \propto \mu^4 \left| \frac{i}{\hbar} \int_0^\infty \langle f|i(t)\rangle \, e^{[i(E_L+E_i+\Gamma)t/\hbar]} dt \right|^2 \tag{2.29}$$

Figure 2.2 is a pictorial representation of the time-dependent approach. In this figure, E_l is the energy of the incident radiation and E_s is the energy of the scattered photons. The RR intensity depends on the time-dependent overlap $\langle f|i(t)\rangle$, where $|i(t)\rangle$ represents the motion of the nuclei upon the transition from the ground to the excited electronic state. Therefore, the time-dependent overlap describes how the geometry of the molecule changes from the ground state equilibrium position to the excited state equilibrium position.

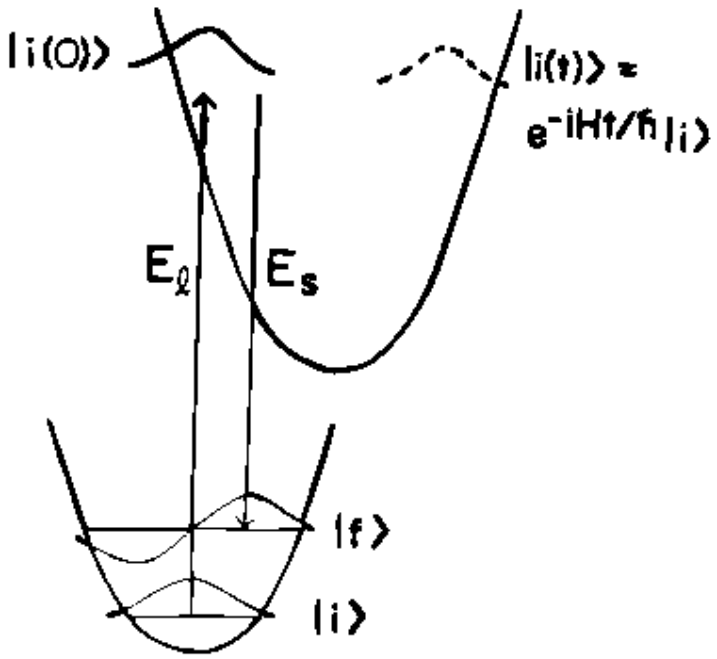

Figure 2.2. Pictorial representation of RR scattering according to the time-dependent approach. Image taken from A. M. Kelly.[53]

2.4 Computational Method

The calculations in this study were computed using the Amsterdam Density Functional (*ADF*) program software.[54,55] The computations in this study employed a Becke Perdew (BP86) exchange correlation functional[56,57] and the triple ζ polarized Slater type (TZP) basis set, except the calculations involving FePImCO used the TZ2P basis set. The vibrational frequencies and normal modes were calculated within the harmonic approximation. The BP86 functional usually produces harmonic frequencies that are close to the experimental data without the utilization of scaling factors.[58] For each system, first the ground state geometry was optimized and subsequently, the excitation energies, vibrational frequencies, Raman spectra, and/or RR spectra were calculated. The excitation energies and oscillator strengths were calculated using the *EXCITATIONS* module of *ADF*.[54] The

dimensionless displacements that are used to calculate the RR intensities were computed using the $VIBRON$ module of ADF.[54] The Franck-Condon factors used to calculated $\Phi(\omega_L)$ are obtained using the two-dimensional array method of Ruhoff and Ratner.[59] We implemented a program to calculate the Franck-Condon factors. Jensen et al. described the procedure used to obtain the RR intensities calculated using the polarizability gradient model.[43] The absolute Raman and RR intensities are given as differential cross-sections. For all of the molecules studied, the sum of the Franck-Condon factors was greater than or equal to 0.96.

Chapter 3

Results

3.1 2-bromo-2-methylpropane

The accuracy of the absolute non-resonance Raman intensities was determined using 2-bromo-2-methylpropane (2B2MP). 2B2MP is a small molecule and there are both experimental and theoretical Raman differential cross-sections for 2B2MP available in the literature. In fact, Le Ru et al.[36] suggested that 2B2MP be used as a standard for experimentally determining the absolute Raman intensities. Table 3.1 compares the DFT results obtained in this study with reported experimental values[41] and also reported DFT results[36] for the Raman differential cross-sections of 2B2MP in vacuum at 633 nm excitation. The reported DFT results were ob-

Table 3.1. Comparison of DFT results with reported experimental values[41] and also reported DFT results[36] for the Raman active modes of 2B2MP at 633 nm excitation. All values correspond to the gas phase of 2B2MP. [a] Frequency in units of cm^{-1}; [b] Depolarization ratio; [c] I in units of $Å^4/amu$; [d] Differential Raman cross-section in units of $10^{-32}cm^2/sr$.

DFT				DFT[36]				Exp.[41]
ν^a	p^b	I^c	$\frac{d\sigma}{d\Omega}{}^d$	ν^a	p^b	I^c	$\frac{d\sigma}{d\Omega}{}^d$	$\frac{d\sigma}{d\Omega}{}^d$
279	0.29	6.37	105	293	0.26	8.97	130	144
483	0.18	22.6	167	509	0.18	23.7	159	169
780	0.68	12.8	50.0	800	0.63	14.3	53.4	44.0

tained using the Gaussian program package[60,61] at the B3LYP[62,63]/6-311++G(d,p) level of theory. As a result of the implementation of different theoretical meth-

ods and basis sets, slight differences are expected between our DFT results and the reported DFT results. Overall, we obtain excellent agreement with both the reported experimental and theoretical results.

3.2 Carbon Disulfide

The accuracy of the absolute RR intensities was determined using CS_2 as a test case. Table 3.2 compares the RR total cross-section of CS_2 in vacuum at 186 nm excitation calculated using the vibronic theory method with a $\Gamma = 0.05$ eV with the experimental[42] RR total cross-section of CS_2 in cyclohexane upon 208.8 nm excitation (the experimental excitation wavelength corresponding to the theoretical excitation wavelength used). Table 3.2 presents the RR intensities as total cross-sections (rather than differential cross-sections). The total cross-section and

Table 3.2. Comparison of DFT results in vacuum at 186 nm excitation with experimental values[42] in cyclohexane at 208.8 nm excitation for the RR total cross-sections of CS_2. The total cross-section is for the fundamental frequency at 652 cm^{-1} and was calculated using vibronic theory with a $\Gamma = 0.05$ eV. [a] Frequency in units of cm^{-1}; [b] RR differential cross-section in units of $10^{-23} cm^2/sr$; [c] RR total cross-section in units of $10^{-23} cm^2$.

DFT			Experimental[42]	
ν^a	$\frac{d\sigma}{d\Omega}{}^b$	σ^c	ν^a	σ^c
652	0.971	10	653	77

differential cross-section are related through the following equation:

$$\sigma = \frac{8\pi}{3}\left(\frac{1+2\rho}{1+\rho}\right)\left(\frac{d\sigma}{d\Omega}\right) \tag{3.1}$$

where σ is the total cross-section and ρ is the depolarization ratio.[64] In converting from the differential cross-section to the total cross-section, the depolarization ratio was assumed to be 1/3 since only one excited state is considered. The RR total cross-section calculated using DFT is about a factor of 8 lower than that obtained experimentally, which is attributed to either solvent effects or exchange correlation functional and basis set effects. Applying the local field correction to the calculated total cross-section in order to take into account the solvent (cyclohexane) effects

results in an increase of the calculated cross-sections by a factor of approximately three. While the calculated total cross-sections are closer to the experimental cross-sections with the local field correction, the calculated cross-sections are still lower than the experimental cross-sections. Thus, it will be necessary to include solvent effects in order to obtain the absolute RR intensities.

3.3 Uracil

Uracil is a six-membered pyrimidine found in RNA.[65] Uracil is a relatively small molecule, making it a suitable system on which to perform quantum mechanical calculations. In addition, there are both experimental[65] and theoretical[43,48,49] studies pertaining to uracil available in the literature. The structure of uracil is shown in Figure 3.1. The theoretical and reported experimental[65] UV absorption spectra

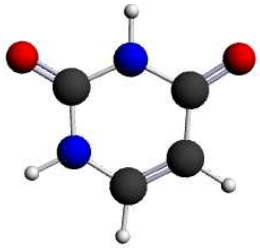

Figure 3.1. Ball and stick model of uracil.

of uracil in vacuum and water, respectively, are shown in Figure 3.2. Both the theoretical and experimental absorption spectra display a single broad band, corresponding to the S_2 state which is dominated by the highest occupied molecular-orbital (HOMO)-lowest unoccupied molecular-orbital (LUMO), a $\pi \rightarrow \pi^*$, transition. Theoretically, the S_2 transition occurs at 262 nm (4.72 eV). However, the

wavelength of maximum absorption occurs at 243 nm (5.10 eV). This shift is a result of the inclusion of vibronic coupling in the calculation of the absorption spectrum. In comparison, the experimental wavelength of maximum absorption is 259 nm (4.79 eV). Differences in the absorption maxima are attributed to solvent effects. The RR spectra are calculated at 262 nm.

We calculated the RR spectra of uracil using three different methods and the results are displayed in Figure 3.3. The absolute RR intensities obtained using the polarizability gradient model, Figure 3.3(a), and the excited state gradient model, Figure 3.3(b), are comparable, which is expected since both of these methods take into consideration only a single excited state. The damping factor is 0.1 eV for both of these spectra.

Additionally, the RR spectrum of uracil was calculated using the vibronic theory with a $\Gamma = 0.1$ eV. Uracil is not expected to be affected by vibronic coupling, as it lacks the presence of vibronic fine structure in the absorption spectrum, indicating that the differential cross-sections obtained using the vibronic theory and short-time approximation should be similar. Indeed, we find that the spectra calculated using both short-time approximation methods, Figures 3.3(a) and 3.3(b), and the vibronic theory, Figure 3.3(c), result in the same relative intensities, but very different absolute intensities. In fact, the vibronic theory method predicts absolute intensities that are a factor of 600 smaller than those calculated using the short-time approximation. This is attributed to the sensitivity of the short-time approximation to the damping parameter. While the absolute RR intensities calculated using the vibronic theory are only slightly impacted by the value of the damping factor, the short-time approximation is extremely sensitive to the value of the damping factor, since the intensities scale as $1/\Gamma^4$. We find that in order for the RR spectrum calculated using the vibronic theory to have the same absolute RR intensities as the RR spectrum calculated using the short-time approximation, the damping factor must be 0.517 eV for the short-time approximation, as shown in Figure 3.3(d). This value of Γ is much larger than expected from the absorption spectra. The value of the damping factor must therefore be selected very carefully for the short-time approximation even when the relative RR intensities are reasonable.

The experimental RR spectrum of uracil in water with 266 nm excitation is

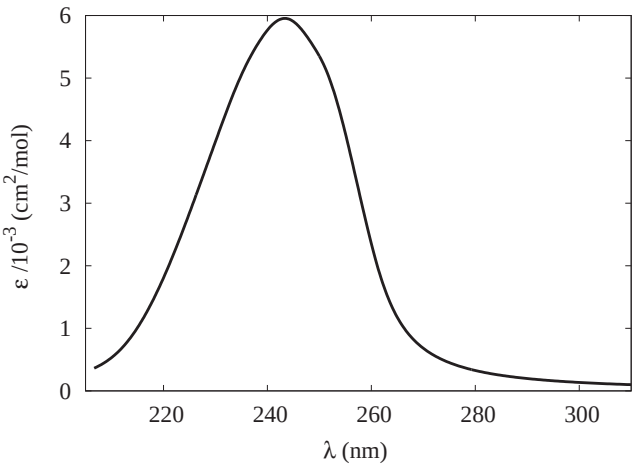

(a) Calculated Absorption Spectrum

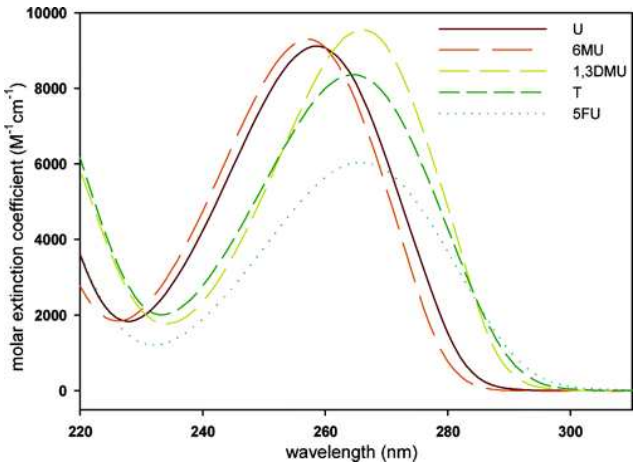

(b) Experimental Absorption Spectrum

Figure 3.2. (a)Calculated absorption spectrum of the S_2 state of uracil in the gas phase. Γ is 0.1 eV. The FCTOT is 0.98. (b) Experimental absorption spectrum of uracil (U), 6-methyluracil (6MU), 1,3-dimethyluracil (1,3DMU), thymine (T), and 5-fluorouracil (5FU) in water at room temperature taken from Gustavssom et al.[65]

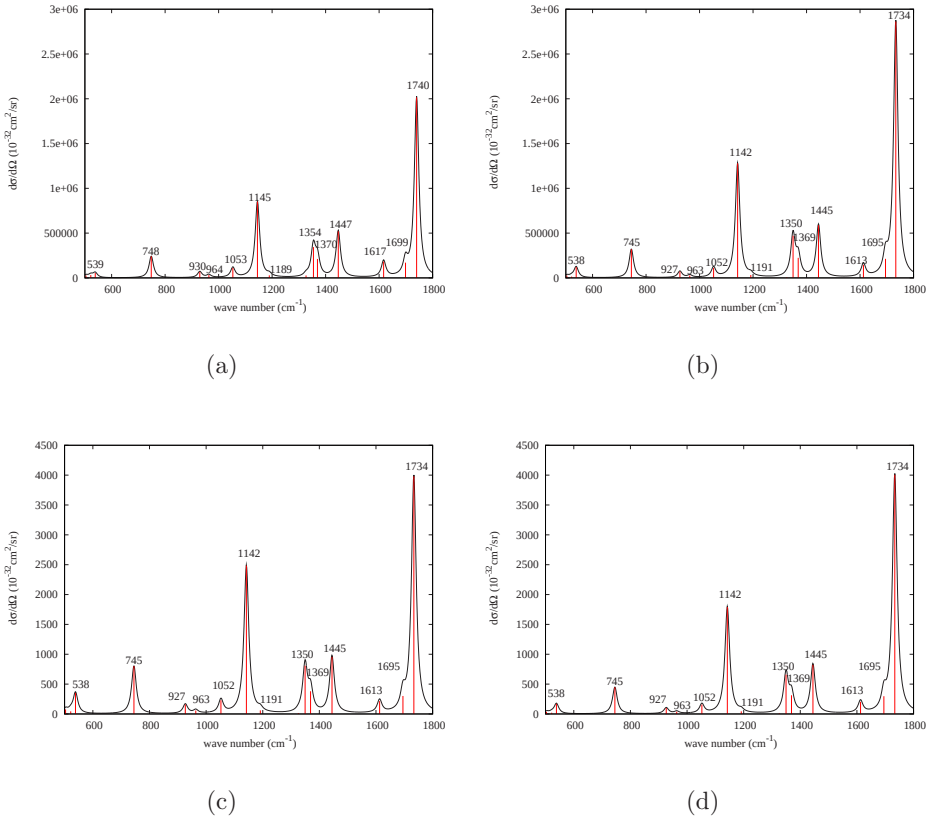

Figure 3.3. Simulated RR spectra of uracil with 262 nm excitation. (a) Calculated using the the short-time approximation within the polarizability gradient model. Γ is 0.1 eV. (b) Calculated using the short-time approximation within the excited state gradient approach. Γ is 0.1 eV. (c) Calculated using the vibronic theory. Γ is 0.1 eV. (d) Calculated using the short-time approximation within the excited state gradient model. Γ is 0.517 eV. RR spectra have been obtained with a Lorentzian having a width of 20 cm^{-1}.

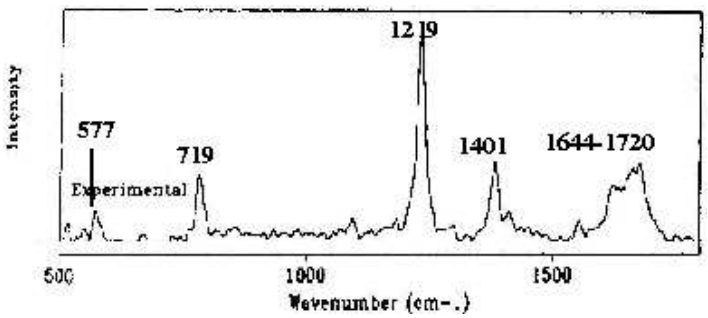

Figure 3.4. Experimental RR spectrum of uracil in water with 266 nm excitation taken from Peticolas and Rush III.[48]

shown in Figure 3.4. There are a few discrepancies between the calculated and experimental RR spectra, especially in the 1600-1800 cm^{-1} region. First, the theoretical RR spectrum presents the peak at 1734 cm^{-1} as much more intense than the corresponding peak at 1720 cm^{-1} in the experimental RR spectrum. This discrepancy in the intensity is attributed to a Fermi resonance.[43,66] More specifically, there is a transfer of intensity to the combination bands of the C-O and N-H bending modes. Under the harmonic approximation, Fermi resonances, combination bands, and overtones are not taken into consideration. In addition, we see two bands at 1350 cm^{-1} and 1445 cm^{-1}, whereas experimentally a single peak at 1401 cm^{-1} is observed in this region. Slight discrepancies are also expected since the theoretical spectrum is calculated in vacuum while the experimental spectrum is obtained in solution. Overall, there is good agreement between the calculated and experimental RR spectra.

The most intense peaks in the RR spectrum occur at 1142, 1350, 1369, and 1734 cm^{-1}. The bands at 1142 and 1350 cm^{-1} correspond to C-N stretching modes. The mode at 1369 cm^{-1} is assigned to a N-H stretching mode. Finally, the band at 1734 cm^{-1} corresponds to a C-O stretching mode.

3.4 Rhodamine 6G

R6G is a cationic dye that contains a xanthene ring substituted with two methyl groups, two ethylamino groups, and a carboxyphenol group. The carboxyphenol group is located nearly perpendicular to the xanthene ring. The structure of R6G is shown in Figure 3.5. Rhodamine 6G (R6G) has been studied by Jensen et al. using time-dependent density functional theory (TD-DFT) to analyze the Raman and RR spectra at an excitation wavelength corresponding to the absorption maximum of the S_1 excitation.[50] However, their model did not account for vibronic coupling effects. Guthmuller and Champagne employed TD-DFT to investigate the RR spectrum of R6G in vacuum and in ethanol for the S_1 and S_3 excited states using both the short-time approximation and vibronic theory.[33] However, they only analyzed the relative RR intensities and did not determine the absolute intensities. Most recently, Shim et al. have experimentally obtained the RR cross-sections of R6G using femtosecond stimulated Raman spectroscopy (FSRS).[35] In

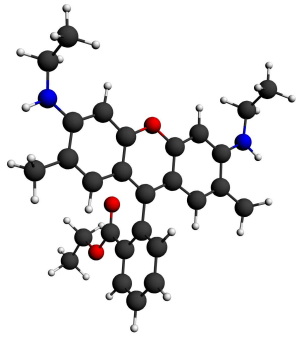

Figure 3.5. Ball and stick model of R6G.

addition, R6G is being used as a prototype molecule in single molecule surface enhanced resonance Raman spectroscopy (SERRS).[67,68] SERRS is a technique that enhances Raman scattering due to both resonance with the electronic transition and also interaction with the metal surface by a factor of 10^{14}-10^{15}, which enables SERRS to be utilized for single molecule detection.[50,67,68]

The calculated and experimental[69] absorption spectra of R6G in vacuum and ethanol, respectively, are shown in Figure 3.6. The calculated absorption spectrum shows a strong band at 473 nm (2.62 eV) corresponding to the $S_0 \rightarrow S_1$ transition. In excellent agreement with our calculation, Jensen and Schatz calculated the S_1 excitation to occur at 474 nm (2.62 eV) using the BP86 functional for R6G in vacuum.[50] The experimental absorption spectrum of R6G in ethanol has a wavelength of maximum absorption at 530 nm (2.34 eV). The theoretical absorption spectrum is slightly blue shifted compared to the experimental spectrum, which can be attributed to solvent effects. Both the calculated and experimental absorption spectra have a weak shoulder, indicating the importance of vibronic coupling effects. The RR spectra are calculated at 473 nm in order to obtain the maximum enhancement.

The Raman bands in an experimental RR spectrum of R6G are concealed by fluorescence. However, theoretical calculation of the RR spectrum of R6G can give us insight about the RR spectrum and the absolute RR intensities. The RR

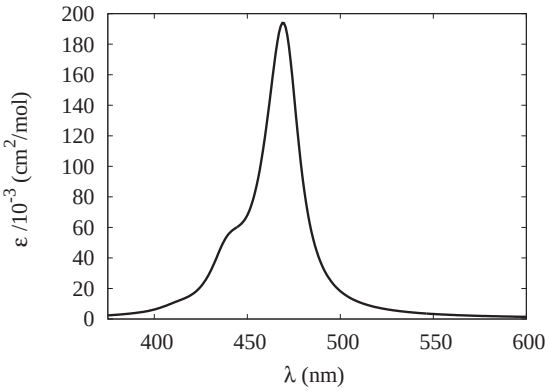

(a) Calculated Absorption Spectrum

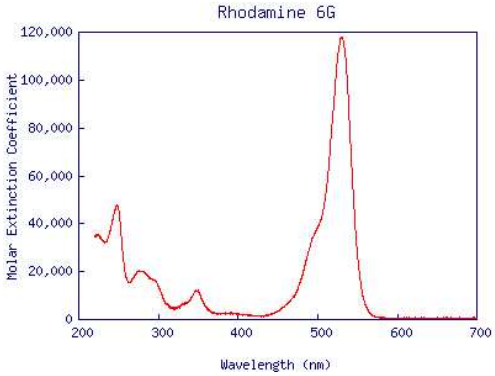

(b) Experimental Absorption Spectrum

Figure 3.6. (a) Calculated absorption spectrum of the S_1 state of R6G. Γ is 0.05 eV. The FCTOT is 0.96. (b) Experimental absorption spectrum of R6G in ethanol obtained from Duh et al.[69] Γ is approximated to be 0.07 eV.

spectra of R6G calculated at 473 nm are shown in Figure 3.7. Figure 3.7(a) is the RR spectrum of R6G calculated using the short-time approximation with Γ=0.07 eV. Figure 3.7(b) is the RR spectrum of R6G calculated using vibronic theory with Γ=0.05 eV. Lastly, Figure 3.7(c) is the RR spectrum of R6G calculated using the short-time approximation with Γ=0.17 eV. Again, the large value of Γ required for the absolute RR intensities calculated using the short-time approximation to agree with those calculated using the vibronic theory demonstrates the sensitivity of the short-time approximation to the damping factor.

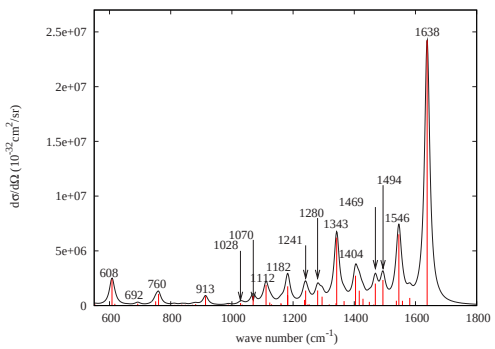

(a) Short-time Approximation, $\Gamma = 0.07$ eV

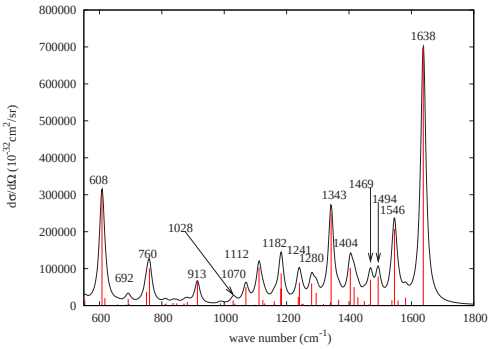

(b) Vibronic Theory Approach, $\Gamma = 0.05$ eV

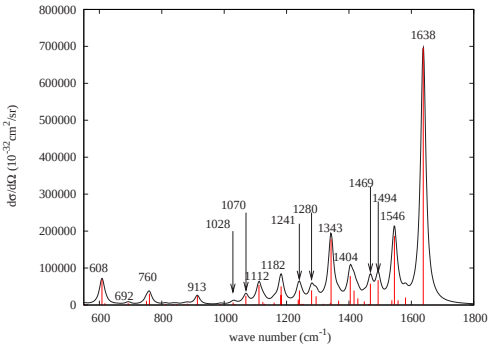

(c) Short-time Approximation, $\Gamma = 0.17$ eV

Figure 3.7. Simulated RR spectrum of rhodamine 6G with 473 nm excitation. (a) Calculated using the short-time approximation. Γ is 0.07 eV. (b) Calculated using vibronic theory. Γ is 0.05 eV. (c) Calculated using the short-time approximation. Γ is 0.17 eV. RR spectra have been broadened with a Lorentzian having a width of 20 cm^{-1}.

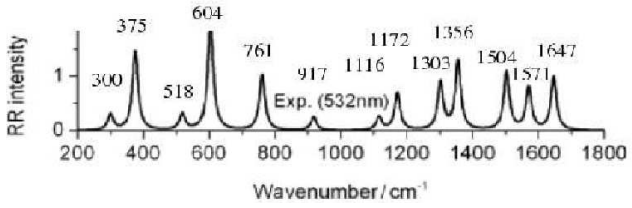

Figure 3.8. Experimental RR spectrum of R6G in methanol with 532 nm excitation from Shim et al.[35]

As expected, the relative intensities of the RR peaks calculated using the short-time approximation and the vibronic theory are not in agreement due to vibronic coupling effects. The low-frequency modes at 608 and 760 cm^{-1} gain intensity compared to the strong peak at 1638 cm^{-1} upon incorporation of vibronic coupling effects. This result agrees with both Guthmuller and Champagne[34] and the experimental spectrum. Guthmuller and Champagne found that the vibronic theory was needed to accurately reproduce the RR spectrum of R6G in resonance with the S_1 excitation. Guthmuller and Champange obtained better agreement with the experimental spectrum because they incorporated solvent and utilized a hybrid functional. The experimental spectrum is shown in Figure 3.8.[35,70] Figure 3.8 only displays the relative RR intensities of R6G in methanol with 532 nm excitation. Calculation of the RR spectra of R6G with both the vibronic theory and the short-time approximation highlights the importance of incorporating vibronic coupling effects into the calculation of the RR spectrum.

Table 3.3 compares the RR total cross-sections calculated at 473 nm using vibronic theory with those obtained experimentally for R6G in methanol at 532 nm (the corresponding transition) from Shim et al.[35] The calculated total cross-

Table 3.3. Comparison of DFT results (gas phase) upon 473 nm excitation with experimental values[35] for the RR cross-sections of R6G in methanol at 532 nm excitation (the corresponding transition). [a] Frequency in units of cm^{-1}; [b] RR differential cross-section in units of $10^{-26} cm^2/sr$; [c] RR cross-section in units of $10^{-23} cm^2$.

DFT			Experimental[35]	
ν^a	$\frac{d\sigma}{d\Omega}{}^b$	σ^c	ν^a	σ^c_{exp}
299	7.77	0.0814	300	0.6±0.1
494	2.52	0.0264	518	0.6±0.1
608	9.43	0.0988	604	4.1±0.5
760	3.17	0.0332	761	2.1±0.3
913	1.97	0.0206	917	0.5±0.09
1112	3.25	0.0340	1116	0.5±0.08
1182	2.73	0.0286	1172	1.4±0.2
1343	7.85	0.0822	1356	2.6±0.3
1546	6.52	0.0683	1571	1.6±0.2
1638	22.0	0.230	1647	2.0±0.3

sections are obtained following the same procedure outlined previously for CS_2. Shim et al. utilized FSRS to obtain the experimental RR total cross-sections

measured using methanol as an internal reference. The calculated total cross-sections are lower than the experimental values by a factor ranging from 10 to 60. Again, this can be attributed to solvent effects or choice of exchange correlation functional and basis set. In addition, since the RR intensities scale as μ^4, even minor underestimations of the transition dipole moments will have a major effect on the total cross-sections.

3.5 Iron(II) Porphyrin with Imidazole and CO Ligands

Iron(II) porphyrin with imidazole and CO ligands (FePImCO) is an ideal model system for larger biologically relevant molecules containing a heme group, such as myoglobin, hemoglobin, or cytochrome c because it mimics the active sites of these heme proteins complexed with carbon monoxide. The structure of FePImCO is shown in Figure 3.9. The structure of metalloporphyrins consists of four pyrrole

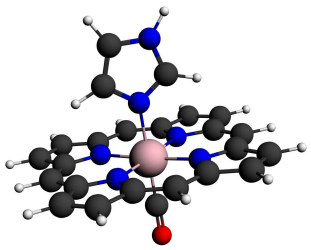

Figure 3.9. Ball and stick model of FePImCO.

groups connected by methine bridges. Each pyrrole group is bonded to the central metal atom through the nitrogen atom.[3] The iron atom sits in the plane of the porphyrin ring and the Fe-C-O bond angle is 180 degrees, which has been reported previously.[71,72] The C-O bond distance is 1.16 Å, the Fe-CO bond distance is 1.76 Å, the Fe-N_{Im} bond distance is 2.07 Å, and the Fe-N_P bond distance is 2.00 Å.

These bond distances are in good agreement with experimental bond distances for Fe(TPP)(CO)(Py) (TPP = tetraphenylporphyrin dianion and Py = pyridine) of 1.12 Å, 1.77 Å, 2.10 Å, and 2.02 Å, respectively[73] and also with theoretically calculated bond distances for FePImCO of 1.165 Å, 1.733 Å, 1.966 Å, and 1.983 Å, respectively.[74]

Metalloporphyrins experience strong absorption in the visible region of the electromagnetic spectrum and are colored complexes due to the highly conjugated tetrapyrrole unit.[3] A weak Q and a strong B (Soret) absorption band are characteristic of metalloporphyrins and can be explained by Gouterman's four-orbital model. Gouterman's four-orbital model describes the Q and B bands as transitions between the close-lying HOMO orbitals, a_{1u} and a_{2u}, and the doubly degenerate LUMO orbitals, e_g. The interaction of the nearly degenerate $a^1_{1u}e^1_g$ and $a^1_{2u}e^1_g$ configurations leads to a high-lying state and also a low-lying state. The B band corresponds to the high-lying state, in which the transition dipoles of the two configurations add together. In contrast, the Q band corresponds to the low-lying state, in which the transition dipoles of the two configurations almost cancel. The B band typically occurs around 380-400 nm and the Q band typically occurs between 500-600 nm.[3,12]

Figure 3.10(a) shows the calculated absorption spectrum of the B band with a Γ = 0.05 eV. The B band is composed of two degenerate excitations, the S_{11} and S_{12} states. The wavelength of maximum absorption is 415 nm (2.99 eV). Therefore, the RR spectrum is calculated at 415 nm in order to obtain maximum enhancement. Figure 3.10(b) shows the calculated absorption spectrum of the Q band with a Γ = 0.05 eV. The Q band is composed of three close-lying excitations, the S_6, S_7, and S_8 states. The wavelength of maximum absorption is 539 nm (2.3 eV). The RR spectrum is therefore calculated at 539 nm. Both the B and Q bands display a shoulder to the blue of the wavelength of maximum absorption, indicating that vibronic coupling will have effects on the RR spectrum.

The RR spectrum of FePImCO calculated using the vibronic theory with a damping factor of 0.05 eV at 415 nm excitation is shown in Figure 3.11(a). The RR spectrum of FePImCO calculated using the short-time approximation with a damping factor of 0.05 eV at 415 nm excitation is shown in Figure 3.11(b). The short-time approximation overestimates the absolute RR intensities. The

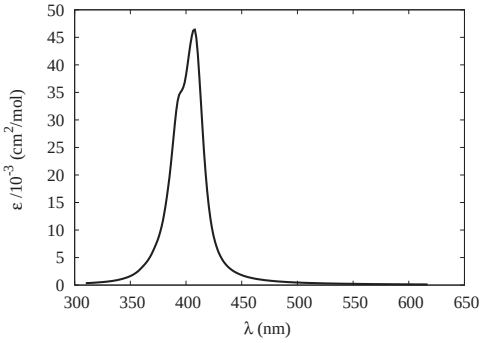

(a) Calculated Absorption Spectrum: B (Soret) Band

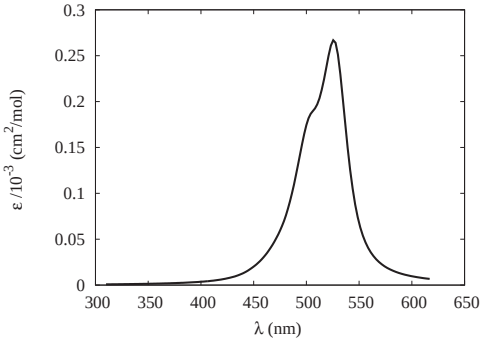

(b) Calculated Absorption Spectrum: Q Band

Figure 3.10. (a) Calculated absorption spectrum of FePImCO for the B (Soret) band. The B band shown here is composed of two degenerate excitations (the 11^{th} and 12^{th} states). The wavelength of maximum absorption is 2.99 eV (415 nm). Γ is 0.05 eV. The FCTOT is 1.00. (b) Calculated absorption spectrum of FePImCO for the Q band. The Q band shown here is composed of three excitations (the 6^{th}, 7^{th}, and 8^{th} states). The wavelength of maximum absorption is 2.3 eV (539 nm). Γ is 0.05 eV. The FCTOT is 0.99.

calculation of the RR spectrum for the B band with the vibronic theory results in an enhancement of the relative intensity of the low-frequency peaks at 353, 527, and 722 cm^{-1}. The experimental RR spectrum for the B band of heme proteins results in strong peaks at 376, 674, and 1373 cm^{-1} due to the vibrations localized in the porphyrin ring.[6] We obtain strong bands at 353, 722, and 1327 cm^{-1}, in good agreement with the experimental results. We calculated Fe-CO stretch to occur at 527 cm^{-1}, in good agreement with the experimental results that report the Fe-CO stretch to occur at 507-512 cm^{-1}.[75]

The RR spectrum of FePImCO calculated using the vibronic theory with a damping factor of 0.05 eV at 539 nm excitation is shown in Figure 3.11(c). The RR spectrum of FePImCO calculated using the short-time approximation with a damping factor of 0.05 eV at 539 nm excitation is shown in Figure 3.11(d). Again, we see that the short-time approximation overestimates the absolute RR intensities. Similar to the RR spectrum calculated at 415 nm excitation, the calculation of the RR spectrum at 539 nm excitation results in an enhancement of the relative intensity of the low-frequency peaks compared to the high-frequency

peaks with the vibronic theory compared to the short-time approximation. The RR peak at 353 cm^{-1} displays the most drastic enhancement in relative intensity. In fact, the peak at 353 cm^{-1} becomes even more intense than the band at 1327 cm^{-1}, which was the most intense peak in the RR spectrum calculated using the short-time approximation. The RR spectra of FePImCO demonstrate the importance of including vibronic coupling effects in the calculation of the RR spectrum and also highlight the shortcomings of the short-time approximation for calculating absolute RR intensities.

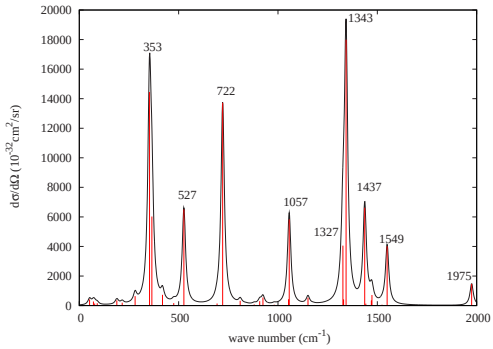

(a) Vibronic Theory: B Band RR spectrum

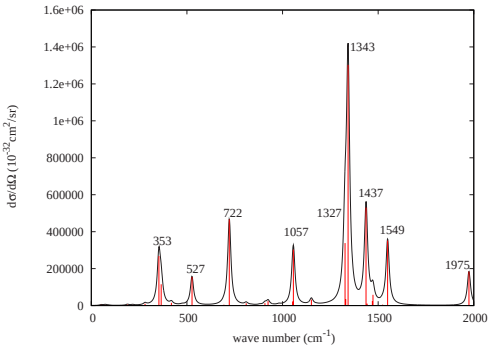

(b) Short-time Approximation: B Band RR spectrum

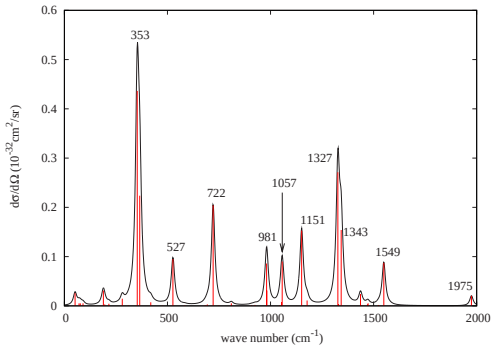

(c) Vibronic Theory: Q Band RR spectrum

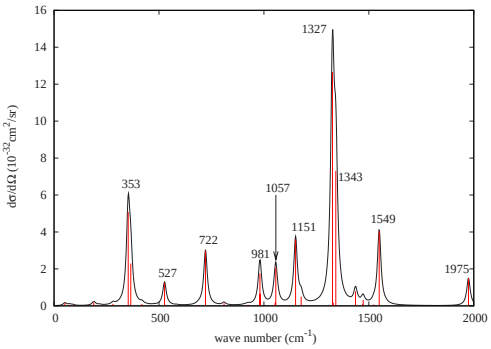

(d) Short-time Approximation: Q Band RR spectrum

Figure 3.11. (a) RR spectrum of FePImCO calculated using vibronic theory for the B band. The B band shown here is composed of two degenerate excitations (the 11^{th} and 12^{th} states). The excitation wavelength is 2.99 eV (415 nm). Γ is 0.05 eV. (b) RR spectrum of FePImCO calculated using the short-time approximation for the B band. The B band shown here is composed of two degenerate excitations (the 11^{th} and 12^{th} states). The excitation wavelength is 2.99 eV (415 nm). Γ is 0.1 eV. (c) RR spectrum of FePImCO calculated using vibronic theory for the Q band. The Q band shown here is composed of three states (the 6^{th}, 7^{th}, and 8^{th} states). The wavelength of maximum absorption is 2.3 eV (539 nm). Γ is 0.05 eV. (d) RR spectrum of FePImCO calculated using the short-time approximation for the Q band. The Q band shown here is composed of three excitations (the 6^{th}, 7^{th}, and 8^{th} states). The wavelength of maximum absorption is 2.3 eV (539 nm). Γ is 0.1 eV. RR spectra have been broadened with a Lorentzian having a width of 20 cm^{-1}.

Chapter 4

Conclusions and Future Directions

This study has been interested in the calculation of absolute RR intensities using DFT. The non-resonance Raman differential cross-sections for 2B2MP calculated using DFT are in excellent agreement with experimental Raman differential cross-sections. The RR total cross-sections calculated for CS_2 and R6G are lower than those obtained experimentally, indicating that DFT underestimates the absolute RR intensities, which is most likely a result of the neglect of solvent effects. However, it is also possible that the choice of exchange correlation functional and basis set resulted in underestimations of the absolute RR intensites. The absolute RR intensities depend on the fourth power of the electronic transition dipole moment, so even small underestimations of the electronic transition dipole moment significantly affects the caclulated absolute RR intensites.

In particular, the two models used to predict the absolute RR intensities were the short-time approximation and the vibronic theory. The short-time approximation was found to severely overestimate the absolute RR intensities in the cases of uracil, R6G, and FePImCO. The intensities calculated using the short-time approximation are very sensitive to the damping factor, whereas, the vibronic theory is less dependent on the damping factor. This makes the vibronic theory more dependable than the short-time approximation.

The vibronic theory has been shown to be necessary for the calculation of the RR spectra of systems affected by vibronic coupling. For the systems analyzed

in this study that are affected by vibronic coupling (i.e. R6G and FePImCO), inclusion of vibronic coupling enhances the relative intensity of the low-frequency modes compared to the high-frequency modes. These enhancements were not detected using the short-time approximation.

Future calculations of the RR spectra could implement the time-dependent approach. This makes sense from a computational perspective because it will result in more efficient calculations of the RR spectra. The vibronic theory method, which involves the sum-over-states computation becomes tedious for large systems that involve many vibrational states.

An additional future direction would be to include solvent in the calculations of the RR spectra, since it is likely that solvent impacts the absolute RR cross-sections. Furthermore, the systems we are interested in investigating model biologically relevant molecules, which usually exist in an aqueous environment. The solvent could be modeled using either explicit water molecules or a solvent continuum model.

Bibliography

[1] Gremlich, H.-U.; Yan, B., Eds.; *Infrared and Raman Spectroscopy of Biological Materials;* Marcel Dekker: New York, 2001.

[2] Siebert, F.; Hildebrandt, P. *Vibrational Spectroscopy in Life Science;* Wiley-VCH: Weinheim, 2008.

[3] Kalyanasundaram, K. *Photochemistry of Polypryridine and Porphyrin Complexes;* volume 28 Academic Press Inc.: San Diego, CA, 1992.

[4] Nelson, D. L.; Cox, M. M. *Lehninger Principles of Biochemistry;* W.H. Freeman: New York, 2004.

[5] Lutz, M. *Biospectroscopy* **1995,** *1,* 313-327.

[6] Hu, S.; Smith, K.; Spiro, T. *J. Am. Chem. Soc.* **1996,** *118,* 12638-12646.

[7] Spiro, T. G. *Resonance Raman Spectroscopy* **1974,** *7,* 339-344.

[8] Spiro, T. G.; Kozlowski, P. M.; Zgierski, M. Z. *J. Raman Spec.* **1998,** *29,* 869-879.

[9] Spiro, T. G.; Kozlowski, P. M. *J. Am. Chem. Soc.* **1998,** *120,* 4524-4525.

[10] Andrade, A.; Misoguti, L.; Neto, N. B.; Zilio, S.; Mendonca, C. *XXVI ENFMC-Annals of Optics* **2003,** *96,.*

[11] Schelvis, Johannes, P.; Deinum, G.; Varotsis, C. A.; Ferguson-Miller, S.; Babcock, G. T. *J. Am. Chem. Soc.* **1997,** *119,* 8409-8416.

[12] Baerends, E.; Ricciardi, G.; Rosa, A.; van Gisbergen, S. *Coordination Chemistry Reviews* **2002,** *230,* 5-27.

[13] Wagner, Richard, W.; Lindsey, J. S.; Seth, J.; Palaniappan, V.; Bocian, D. F. *J. Am. Chem. Soc.* **1996,** *118,* 3996-3997.

[14] Rochford, J.; Chu, D.; Hagfeldt, A.; Galoppini, E. *J. Am. Chem. Soc.* **2007,** *129,* 4655-4665.

[15] Rochford, J.; Galoppini, E. *Langmuir* **2008,** *24,* 5366-5374.

[16] Lewis, I. R.; Edwards, H. G. *Handbook of Raman Spectroscopy;* Marcel Dekker, Inc.: New York, NY, 2001.

[17] Long, D. A. *The Raman Effect;* John Wiley & Sons, Inc.: New York, 2002.

[18] Albrecht, A. *J. Chem. Phys.* **1961,** *34,* 1476-1484.

[19] Tang, J.; Albrecht, A. *J. Chem. Phys.* **1968,** *49,* 1144-1154.

[20] Albrecht, A.; Hutley, M. *J. Chem. Phys.* **1971,** *55,* 4438-4443.

[21] Heller, E.; Sundberg, R.; Tannor, D. *J. Phys. Chem.* **982,** *86,* 1822-1833.

[22] Myers, A. B. *Chem. Rev.* **1996,** *96,* 911-926.

[23] Lee, S.; Heller, E. *J. Chem. Phys.* **1979,** *71,* 4777-4788.

[24] Heller, E. *Acc. Chem. Res.* **1981,** *14,* 368-375.

[25] Spiro, T. G. *J. Am. Chem. Soc.* **1974,** *7,* 339-344.

[26] Fodor, S. P.; Rava, R. P.; Hays, T. R.; Spiro, T. G. *J. Am. Chem. Soc.* **1989,** *107,* 1520-1529.

[27] Song, S.; Asher, S. A. *J. Am. Chem. Soc.* **1974,** *111,* 4295-4305.

[28] Arnaud, C. H. *Chemical & Engineering News* **2009,** *87,* 10-14.

[29] Jorio, A.; Fantini, C.; Dantas, M.; Pimenta, M.; Filho, A. S.; Samsonidze, G.; Brar, V.; Dresselhaus, G.; Dresselhaus, M.; A.K., S.; Ünlü, M.; Goldberg, B.; Saito, R. *Phys. Rev. B* **2002,** *66,* 115411.

[30] Jorio, A.; Santos, A.; Ribeiro, H.; Fantini, C.; Souza, M.; Vieira, J.; Furtado, C.; Jiang, J.; Saito, R.; Balzano, L.; Resasco, D.; Pimenta, M. *Phys. Rev. B* **2005,** *72,* 075207.

[31] Dresselhaus, M.; Eklund, P. *Advances in Physics* **2000,** *49,* 705-814.

[32] Brown, C. W.; Ferraro, J. R.; Nakamoto, K. *Introductory Raman Spectroscopy;* Academic Press Inc.: USA, 2003.

[33] Guthmuller, J.; Champagne, B. *J. Phys. Chem. A* **2008,** *112,* 3215-3223.

[34] Guthmuller, J.; Champagne, B. *J. Chem. Phys.* **2007,** *127,* 164507.

[35] Shim, S.; Stuart, Christina, M.; Mathies, R. A. *Comput. Phys. Commun.* **2008,** *9,* 697-699.

[36] Le Ru, E. C.; Blackie, E.; Meyer, M.; Etchegoin, P. *J. Phys. Chem. C* **2007,** *111,* 13794-13803.

[37] Negri, F.; di Donato, E.; Tommasini, M.; Castiglioni, C.; Zerbi, G.; Mullen, K. *J. Chem. Phys.* **2004,** *120,* 11889-11900.

[38] Warshel, A.; Dauber, P. *J. Chem. Phys.* **1977,** *66,* 5477-5488.

[39] Johnson, B.; Peticolas, W. *Ann. Rev. Phys. Chem.* **1976,** *27,* 465-521.

[40] Neugebauer, J.; Baerends, E.; Efremov, E.; Ariese, F.; Gooijer, C. *J. Phys. Chem. A* **2005,** *109,* 2100-2106.

[41] Schrotter, H.; Kloeckner, H. Raman scattering cross sections in gases and liquids. In *Raman Spectroscopy of Gases and Liquids*, Vol. 11; Weber, A., Ed.; Springer-Verlag Berlin: Heidelberg, Germany, 1979.

[42] Myers, A. B.; Li, B.; Ci, X. *J. Chem. Phys.* **1988,** *89,* 161876.

[43] Jensen, L.; Zhao, L. L.; Autschbach, J.; Schatz, G. C. *J. Chem. Phys.* **2005,** *123,* 174110.

[44] Kramers, H.; Heisenberg, W. *Z. Phys.* **1925,** *31,* 681-708.

[45] Dirac, P. *Proc. R. Soc. (London)* **1927,** *114,* 710-728.

[46] Hizhnyakov, V.; Tehver, I. *Phys. Status Solidi* **1967,** *21,* 755-768.

[47] Blazej, D. C.; Peticolas, W. L. *J. Chem. Phys.* **1980,** *72,* 3134-3142.

[48] Peticolas, W. L.; Rush III, T. *J. Comp. Chem.* **1995,** *16,* 1261-1271.

[49] Neugebauer, J.; Hess, B. A. *J. Chem. Phys.* **2004,** *120,* 11564.

[50] Jensen, L.; Schatz, G. C. *J. Phys. Chem. A* **2006,** *110,* 5973-5977.

[51] Lilichenk, M.; Tittelbach-Helmrich, D.; Verhoeven, J. W.; Gould, I. R.; Myers, A. B. *J. Chem. Phys.* **1998,** *109,* 10958.

[52] Biswas, N.; Umpathy, S. *J. Chem. Phys.* **2003,** *118,* 5526-5537.

[53] Kelly, A. M. *J. Phys. Chem. A* **1999,** *103,* 6891-6903.

[54] Baerends, E.; Autschbach, J.; Berces, A.; Bo, C.; Boerrigter, P.; Cavallo, L.; Chong, D.; Deng, L.; Dickson, R.; Ellis, D. E. e. a. "Amsterdam density functional", http://www.scm.com, 2008.

[55] te Velde, G.; Bickelhaupt, F.; Baerends, E.; Guerra, C. F.; van Gisbergen, S.; Snijders, J.; Ziegler, T. *J. Comp. Chem.* **2001,** *22,* 931-967.

[56] Becke, A. *Phys. Rev. A* **1988,** *38,* 3098-3100.

[57] Perdew, J. *Phys. Rev. B* **1986,** *33,* 8822-8824.

[58] Neugebauer, J.; Hess, B. A. *J. Chem. Phys.* **2003,** *118,* 7215-7225.

[59] Ruhoff, P. T.; Ratner, M. A. *Int. J. Quant. Chem.* **2000,** *77,* 383-392.

[60] Frisch, M. *et al.* "Gaussian 03", http://www.gaussian.com/, 2003 Gaussian, Inc., Wallingford CT 2003.

[61] Frisch, M. *et al.* "Gaussian; Technical Report", 2003.

[62] Becke, A. *J. Chem. Phys.* **1993,** *98,* 5648-5652.

[63] Lee, C.; Yang, W.; Parr, R. *Phys. Rev. B* **1988,** *37,* 785-789.

[64] Li, B.; Myers, A. B. *J. Phys. Chem.* **1990,** *94,* 4051-4054.

[65] Gustavssom, T.; Bnysz, k.; Lazzarotto, E.; Markovitsi, D.; Scalmani, G.; Frisch, M. J.; Barone, V.; Improta, R. *J. Am. Chem. Soc.* **2006,** *128,* 607-619.

[66] Szczesniak, M.; Nowak, M.; Rostkowska, H.; Szxzepaniak, K.; Person, W.; Shugar, D. *J. Am. Chem. Soc.* **1983,** *105,* 5969-5976.

[67] Hildebrandt, P.; Stockburger, M. *J. Phys. Chem.* **1984,** *88,* 5935-5944.

[68] Michaels, A.; Nirmal, M.; Brus, L. *J. Am. Chem. Soc.* **1999,** *121,* 9932-9939.

[69] Du, H.; Fuh, R.; Li, J.; Corkan, A.; Lindsey, J. *Photochemistry and Photobiology* **1998,** *68,* 141-142.

[70] Guthmuller, J.; Champagne, B. *Comput. Phys. Commun.* **2008,** *9,* 1667-1669.

[71] Rovira, C.; Kunc, K.; Hutter, J.; Pietro, B.; Parrinello, M. *J. Quantum Chemistry* **1997,** *69,* 31-35.

[72] Ohta, T.; Pal, B.; Kitagawa, T. *J. Phys. Chem. B* **2005,** *109,* 21110-21117.

[73] Peng, S.-M.; Ibers, J. A. *J. Am. Chem. Soc.* **1976,** *98,* 8032-8036.

[74] Ghosh, A.; Bocian, D. F. *J. Chem. Phys.* **1996,** *100,* 6363-6367.

[75] Tsubaki, M.; Srivastava, R.; Yu, N. *Biochemistry* **1982,** *21,* 1132-1140.